

Evolution of the turbulence structure in the surf and swash zones

IN MEI SOU¹†, EDWIN A. COWEN²
AND PHILIP L.-F. LIU^{2,3}

¹Department of Civil and Environmental Engineering, University of Hawaii at Manoa, Honolulu, HI 96822, USA

²DeFrees Hydraulics Laboratory, School of Civil and Environmental Engineering, Cornell University, Ithaca, NY 14853, USA

³Institute of Hydrological and Oceanic Sciences, National Central University, Jongli, Taoyuan 32001, Taiwan

(Received 12 November 2008; revised 16 September 2009; accepted 18 September 2009)

The velocity field and turbulence structure within the surf and swash zones forced by a laboratory-generated plunging breaking wave were investigated using a particle image velocimetry measurement technique. Two-dimensional velocity fields in the vertical plane from 200 consecutive monochromatic waves were measured at four cross-shore locations, shoreward of the breaker line. The phase-averaged mean flow fields indicate that a shear layer occurs when the uprush of the bore front interacts with the downwash flow. The turbulence characteristics were examined via spectral analysis. The larger-scale turbulence structure is closely associated with the breaking-wave- and the bore-generated turbulence in the surf zone; then, the large-scale turbulence energy cascades to smaller scales, as the turbulent kinetic energy (TKE) evolves from the outer surf zone to the swash zone. Smaller-scale energy injection during the latter stage of the downwash phase is associated with the bed-generated turbulence, yielding a -1 slope in the upper inertial range in the spatial spectra. Depth-integrated TKE budget components indicate that a local TKE equilibrium exists during the bore-front phases and the latter stage of the downwash phases in the outer surf zone. The TKE decay resembles the decay of grid turbulence during the latter stage of the uprush and the early stage of the downwash, as the production rate is small because of the absence of strong mean shear during this stage of the wave cycle as well as the relatively short time available for the growth of the bed boundary layer.

1. Introduction

Erosion and accretion are natural processes caused by waves and currents in the coastal zone. Most beach erosion or accretion takes place within the swash zone (Beach & Sternberg 1992), the inner portion of the surf zone, in which wave run-up periodically covers and uncovers the beach face. The hydrodynamics in this region is complex and is still not well understood, although it has significant impact on our coasts. It is difficult to fully model the boundary-dominated swash zone flows with fundamental mass, momentum and energy transport equations because of the strong

† Email address for correspondence: isou@hawaii.edu

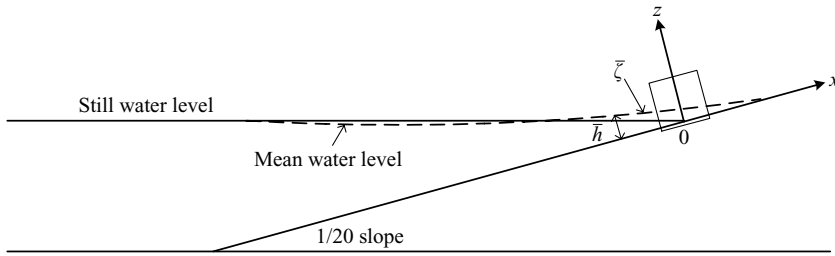
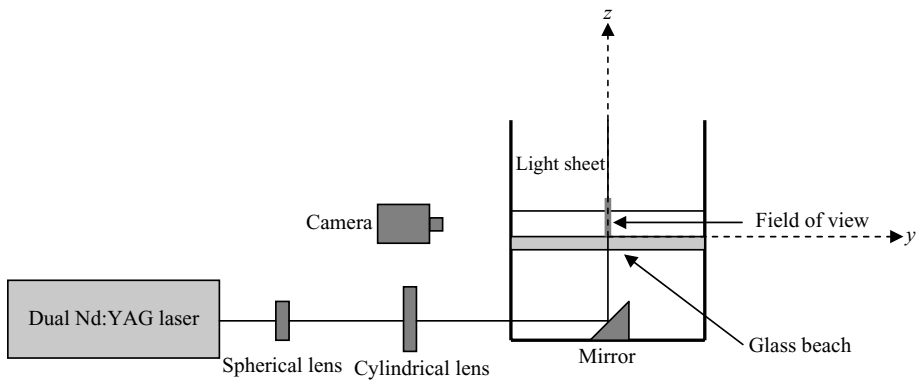
turbulence and the complexity of boundary conditions, namely the mobile bed, the multi-phased flows and the dynamic free surface. Furthermore, it is difficult to make field measurements in thin and aerated flows in the swash zone.

Many laboratory studies in the surf and swash zones have relied on laser Doppler velocimetry (LDV) measurements. Nadaoka & Kondoh (1982) investigated the velocity field within the surf zone to clarify the dependence of sand movement on the near-bed velocity using an LDV technique. They found the coexistence of large-scale turbulence from surface sources (the breaking wave) and small-scale bottom-generated turbulence. Ting & Kirby (1994, 1995, 1996) used LDV to investigate the differences in the surf zone turbulence characteristics forced by plunging and spilling breakers. They found that turbulent kinetic energy (TKE) is transported seaward under a spilling breaker and landward under a plunging breaker. Pedersen, Deigaard & Sutherland (1998) successfully used two LDV measurement systems to investigate turbulence length scales using spatial correlation between velocity measurements in the surf zone. They found that the integral length scale grows linearly with distance from the bed. Recently, Feng & Stansby (2005) and Stansby & Feng (2005) used LDV to investigate the flow structure of a spilling breaker, identifying divergence and convergence points from the streamlines of the flow field in the surf zone.

In the swash zone, Hwung *et al.* (1998) and Petti & Longo (2001) were able to study the vertical turbulence structure in the swash zone using LDV. Their definition of the swash zone moves it further offshore, into the inner surf zone. In the present study, the swash zone is defined as the region within the moving shoreline, i.e. the region that is dry at some point within the periodic wave cycle.

Unlike the point measurement techniques utilized in previous laboratory and field studies in the surf and swash zones, the particle image velocimetry (PIV) technique provides full-field two-dimensional instantaneous velocity fields. Thus, PIV allows a detailed turbulence analysis, as the TKE production and dissipation rates can be directly evaluated with the spatial gradients obtained from the instantaneous velocity fields. Previous studies of the TKE budget of breaking waves are relatively few because of the difficulty in estimating the production and dissipation terms. Traditional LDV measurements cannot evaluate instantaneous spatial gradients. For the PIV studies, the measurement region of the studies of Chang & Liu (1999) and Melville, Veron & White (2002) are large (of the order of 10 cm) relative to the dissipative turbulence length scales. Chang & Liu (1999) evaluated the dissipation term by balancing the TKE evolution equation with other terms. Melville *et al.* (2002) used PIV to examine the TKE budget of breaking waves in an open channel (i.e. not on a sloping beach). They showed that the turbulence under the breaking wave is locally isotropic in the open channel (the water depth is not as shallow as in the inner surf and swash zones); thus, the dissipation could be evaluated as $15\nu\langle(\partial u/\partial x)^2\rangle$ (Tennekes & Lumley 1972), in which ν is kinematic viscosity and $\partial u/\partial x$ is the horizontal velocity gradient in the direction of wave propagation. Cowen *et al.* (2003) used a PIV technique to quantify the evolution of TKE and dissipation of plunging- and spilling-forced swash zones in the laboratory. The temporal TKE decay was found to behave similarly as grid turbulence decay during the latter stage of uprush and the early stage of the downwash.

Different from our earlier paper (Cowen *et al.* 2003), which examined the difference between plunging- and spilling-forced swash zones at one measurement location, in this effort the evolution of the turbulence structure is examined from the outer surf to the swash zones at four different locations for a plunging wave case. First, we describe the experiments and data analysis methods in §2. The turbulence characteristics of the surf and swash zones are investigated via spectral analysis in §3.1. The evolution of the


 FIGURE 1. Experiment coordinate system (x - z plane).

 FIGURE 2. Schematic of the experimental set-up viewed from the end of the wave tank (y - z plane).

TKE is presented in § 3.2. The importance of bore-generated turbulence is discussed with a comparison between the TKE and turbulence production in § 3.2.1. A detailed look at the TKE and turbulence dissipation is presented in § 3.2.2. Production and dissipation are analysed and discussed in § 3.2.3. Finally, the overall TKE budget from the surf zone to the swash zone is presented in § 3.2.4. The conclusions are presented in § 4.

2. Experimental set-up and data analysis

The surf and swash zones were generated in a wave tank (32 m long, 0.6 m wide and 0.9 m deep) with painted steel bottom and glass sidewalls in the DeFrees Hydraulics Laboratory of Cornell University. A piston-type wavemaker is located at one end of the tank, and a 1:20 slope glass beach is at the other end. The wavemaker is driven hydraulically and controlled by a computer to generate monochromatic waves. We define our coordinate system such that x is positive onshore along the beach face. The location $x = 0$ is placed at the intersection of the still water level with the beach. The z direction is defined normal to the beach face and positive upward. The y axis is set by the right-hand rule with $y = 0$ at the lateral mid-point of the tank as shown in figures 1 and 2.

We set the offshore water depth at 26.0 cm and generated a monochromatic wave with period $T = 2.0$ s. The incident wave height was $H = 2.46$ cm, which was measured 9 m from the wavemaker, using a capacitance-type wave gauge. The wave condition generated a plunging breaker characterized by the surf similarity parameter $\xi = S/\sqrt{H/\lambda} = 0.56$ (Battjes 1974), where S is the beach slope and λ is the wavelength,

	Centred at x	Area	Spatial resolution of calculated velocity field
\mathcal{A}_1	-55.0 cm	7.70 cm by 7.70 cm	0.631 mm
\mathcal{A}_2	-30.0 cm	5.05 cm by 5.05 cm	0.414 mm
\mathcal{A}_3	0.0 cm	3.00 cm by 3.00 cm	0.246 mm
\mathcal{A}_4	17.5 cm	2.85 cm by 2.85 cm	0.234 mm

TABLE 1. Area and spatial resolution of the measurement locations.

determined from the dispersion relation using the water depth and wave period. The detailed experimental set-up and procedure are outlined in Cowen *et al.* (2003) and Sou (2006). The experiments were repeated four times in order to make PIV measurements at four different cross-shore locations. The measurement area was locally seeded with fluorescent particles. An optical filter (Tiffen 21 Orange lens) was used to ensure that only light emitted by the fluorescent particles was imaged and, importantly, not the light scattered by the air bubbles. The camera was computer controlled to acquire 6000 consecutive image pairs (12 000 images) at 15 Hz, yielding 200 resolved consecutive wave periods. Because of the different local water depths, the image size varies from the offshore location to the onshore location with decreasing size in the field of view (FOV). Three measurement areas are within the surf zone, while one measurement area is within the swash zone. As shown in table 1, we refer to the four measurement areas as \mathcal{A}_1 (centred at $x = -55$ cm), \mathcal{A}_2 (centred at $x = -30$ cm), \mathcal{A}_3 (centred at $x = 0$ cm, the still water line) and \mathcal{A}_4 (centred at $x = 17.5$ cm).

The time average of any temporally varying quantity $\Theta(t)$ over a time interval \tilde{T} is defined as

$$\bar{\Theta} = \frac{1}{\tilde{T}} \int_0^{\tilde{T}} \Theta(t') dt'. \quad (2.1)$$

The phase average of a temporally periodic quantity, with replication period T and total temporal length $\tilde{T} = NT$, where N is the number of periods in the record (which is 200 in the present case), is defined as

$$\langle \Theta(\tau) \rangle = \frac{1}{N} \sum_{n=0}^{N-1} \Theta(\tau + nT), \quad \text{where } \tau \text{ lies in the interval } \{0, T\}. \quad (2.2)$$

Given $T = 2$ s and the PIV data rate of 15 Hz, 30 wave phases were resolved within each wave period. The instantaneous perturbation $\Theta'(t)$ is defined as

$$\Theta'(t) = \Theta(t) - \langle \Theta(t) \rangle \quad (2.3)$$

and the perturbation intensity as $\langle \Theta'^2(t) \rangle^{1/2}$.

The free-surface profile for each instantaneous velocity field was obtained directly from the first raw image in each image pair. Six points on the free surface were obtained by manual interrogation, using the reflections of the fluorescent particles created by the free surface. A third-order polynomial was fit to the six points in a least square sense, yielding a continuous estimate of the instantaneous free-surface position for each image pair. Detailed investigation of the velocity field near the free surface is challenging owing to the local uncertainty in free-surface position at the bore-front phases, as the free surface is not itself discernible because of the use of

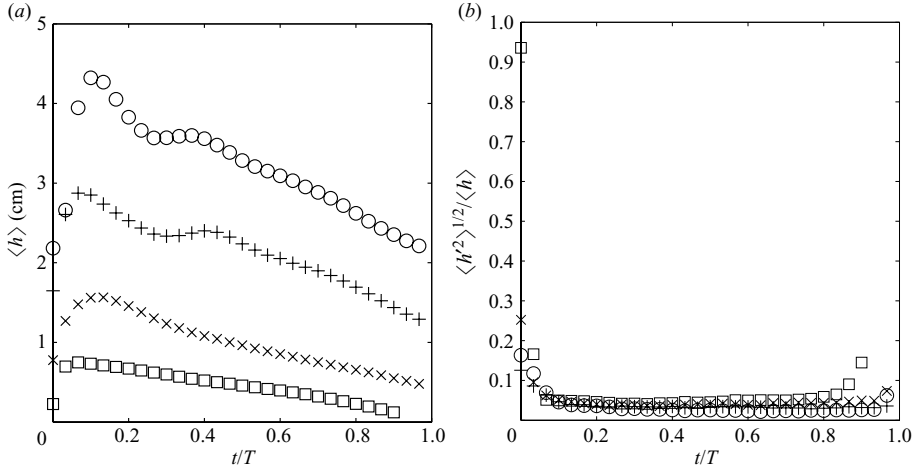


FIGURE 3. (a) The phase-averaged water depth $\langle h \rangle$ and (b) the ratio of the root-mean-square free-surface deviation to the phase-averaged water depth averaged across the FOV (i.e. averaged in the cross-shore direction) $\langle h'^2 \rangle^{1/2} / \langle h \rangle$ at the measurement locations: \circ , \mathcal{A}_1 ; $+$, \mathcal{A}_2 ; \times , \mathcal{A}_3 ; \square , \mathcal{A}_4 .

the optical filter. Hence, in this paper, we will focus on the bulk water column and near-bed turbulence.

Our turbulence decomposition (2.3) assumes a high period-to-period repeatability. To test the repeatability, we phase averaged the determined free-surface profiles at each cross-shore location. We defined the first uprush phase ($t/T = 0$) at each cross-shore location to be the phase at which the bore front first enters the measurement area. Uprush phases are the phases when the flow is directed up the beach, while downwash phases are the phases when the flow retreats in the offshore direction.

The ratio of $\langle h'^2 \rangle^{1/2}$ to $\langle h \rangle$ averaged in the x direction within the FOV at each cross-shore location is shown in figure 3. The figure indicates that the wave is highly repeatable except at the bore-front arrival, where it has a higher level of $\langle h'^2 \rangle^{1/2}$ indicating some wave-to-wave variation when the bore front passes through the measurement region. Based on our own observations this is due to both subtle changes in the arrival time of the bore front and variations in its arrival amplitude and shape. After breaking, the broken wave produces higher-frequency components with random phase on the free surface, and this contributes to the higher unsteadiness in the free-surface position during the uprush stage while remaining quite repeatable at longer wavelengths. The energy spectra of the incident wave measured at 8 m and 9 m from the wavemaker (figure 4) indicate that no low-frequency components of wave energy exist at our wave condition. This demonstrates that no unwanted long-wave noise was present. The wave reflection coefficient was determined using the wave envelope method (Dean & Dalrymple 1991) and was found to be 0.041. This, along with the negligible $\langle h'^2 \rangle^{1/2}$, indicates that the reflection from the beach is negligible for our experiments.

The images were post-processed for instantaneous velocity, using a central-difference (Werelely & Meinhardt 2001) form of the dynamic sub-window PIV technique outlined in Cowen & Monismith (1997). Images were initially interrogated with a 64×64 pixel sub-window with a 50% overlap. Spurious vectors at a given point in space and time (phase) were removed using a combination of a local median filter (Westerweel

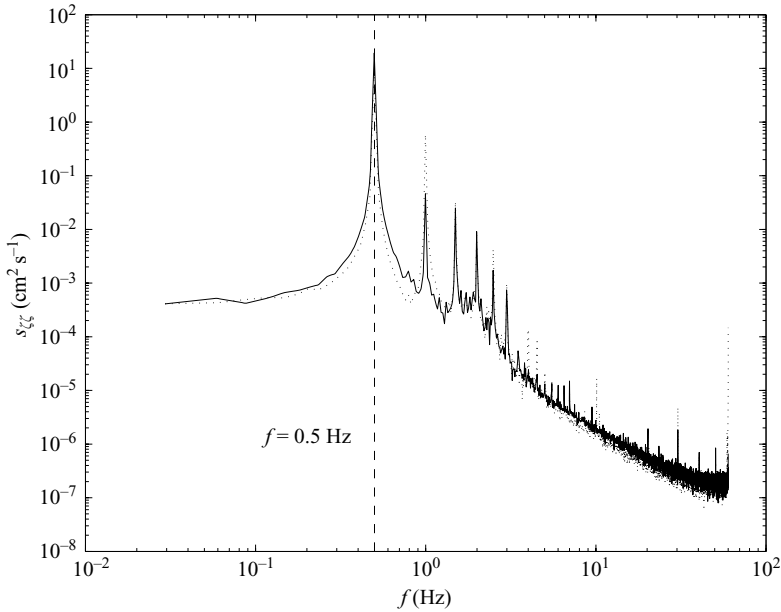


FIGURE 4. Incident wave energy spectra measured at 8 m and 9 m from the wavemaker: \cdots , 8 m; —, 9 m.

1994) for space and an adaptive Gaussian filter (Cowen & Monismith 1997) for time (phase). The means of the resulting filtered displacements were then used as initial estimates of sub-window displacements for a second processing of the image pairs, at a reduced sub-window size of 32×32 pixels with a 75% overlap. The image pairs were processed a third and a fourth time, using the filtered instantaneous displacements of the previous analysis pass again with a 32×32 pixel sub-window and a 75% overlap, resulting in a 122×122 grid of velocity vectors for each instantaneous velocity field. Required missing displacements (because of removal by the spurious vector filter or as a result of interrogation resolution changes) were obtained by linear interpolation on a Delaunay triangular mesh connecting the valid displacement interrogation points. As the FOV varies at each cross-shore location, the vertical and horizontal resolution of the PIV data varies as shown in table 1.

The instantaneous free surface evinces some wave-to-wave variation, and the phase average is constructed based only on velocity vectors located below the instantaneous free surface. This phase-averaging method is a conditional form of that described by (2.2). As a result, the number of valid instantaneous velocity vectors used in the phase average at any interrogation point can be less than the total number of image pairs (200), particularly near the free surface. The phase-averaged free-surface profile is defined as the line at which 50% of the 200 instantaneous velocity vectors at the same phase are valid. Note that the still water surface is not aligned with the x direction because of the definition of our coordinate system. An example of the distribution of the number of valid velocity vectors with the corresponding phase-averaged velocity vector field is shown in figure 5 ($t/T = 0$ at \mathcal{A}_3).

Bootstrap uncertainty analysis (Efron & Tibshirani 1991) was used to find the 95% confidence intervals of the calculated metrics from 2000 bootstrap data samples. The confidence intervals of the measured quantities are expected to be correlated to the wave-to-wave repeatability; hence, the bore-front phase is expected to have higher

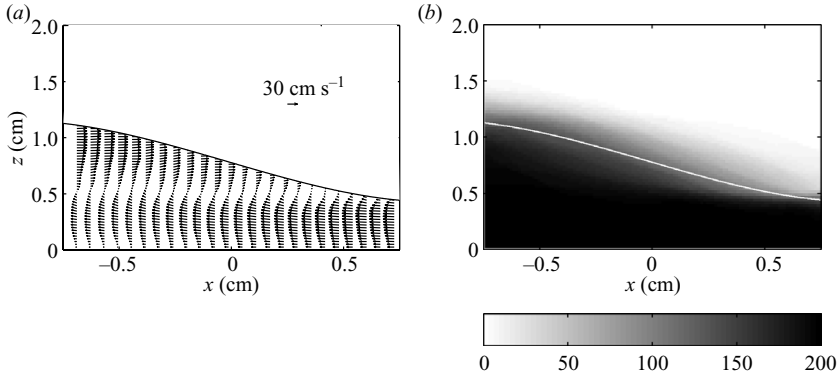


FIGURE 5. An example of the distribution of the valid vectors ($30t/T=0$) at \mathcal{A}_3 : (a) phased-averaged velocity vectors; (b) number of valid instantaneous velocity vectors; the solid line is the phase-averaged free surface.

$\frac{z}{h}$	\bar{u} (cm s ⁻¹)	\bar{w} (cm s ⁻¹)	$\overline{u^2}$ (cm s ⁻¹)	$\overline{w^2}$ (cm s ⁻¹)
0.9	20.49 -1.72, +1.64	0.642 -0.287, +0.291	1.49 -0.26, +0.27	1.34 -0.23, +0.23
0.5	9.94 -0.86, +0.84	0.893 -0.268, +0.273	1.28 -0.22, +0.24	1.11 -0.18, +0.20
0.1	-18.8 -0.5, +0.5	1.05 -0.20, +0.20	2.59 -0.30, +0.32	1.08 -0.12, +0.13

TABLE 2. Representative 95 % confidence intervals during uprush at $t/T=0$ at \mathcal{A}_3 .

$\frac{z}{h}$	\bar{u} (cm s ⁻¹)	\bar{w} (cm s ⁻¹)	$\overline{u^2}$ (cm s ⁻¹)	$\overline{w^2}$ (cm s ⁻¹)
0.9	-27.6 -0.2, +0.2	-0.097 -0.057, +0.057	1.12 -0.12, +0.12	0.304 -0.037, +0.039
0.5	-26.5 -0.2, +0.2	-0.058 -0.042, +0.041	1.10 -0.12, +0.12	0.220 -0.027, +0.029
0.1	-19.0 -0.2, +0.2	-0.057 -0.052, +0.052	1.26 -0.14, +0.15	0.268 -0.035, +0.037

TABLE 3. Representative 95 % confidence intervals during uprush at $30t/T=27$ at \mathcal{A}_3 .

uncertainty. Representative confidence intervals at the bore-front phase ($t/T=0$) are shown in table 2 and at a typical downwash phase ($30t/T=27$) are shown in table 3.

As expected the confidence intervals during the bore-front phase are broader than during the downwash phase. Based on the local maximum horizontal mean velocity the typical uncertainty in mean quantities is seen to be less than 1 %, while based on the local maximum turbulence intensity the typical uncertainty is approximately 10 %.

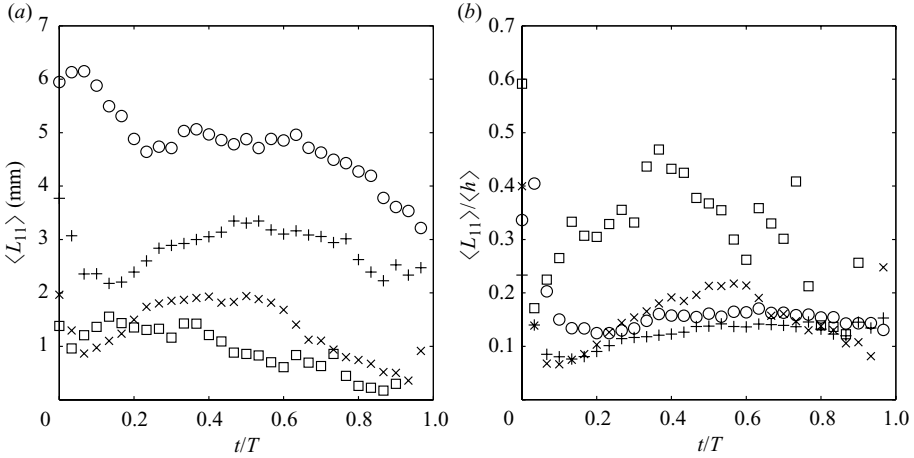


FIGURE 6. (a) Variations of the longitudinal integral length scale $\langle L_{11} \rangle$ and (b) the normalized longitudinal integral length scale $\langle L_{11} \rangle / \langle h \rangle$ over the wave cycle at the four measurement locations: \circ , \mathcal{A}_1 ; $+$, \mathcal{A}_2 ; \times , \mathcal{A}_3 ; \square , \mathcal{A}_4 .

3. Results

3.1. Turbulence characteristics

An advantage of the PIV technique is that spatial spectral analysis is possible without invoking the Taylor frozen turbulence hypothesis (Taylor 1938), which is required to investigate wavenumber spectra in point-measurement turbulence studies (e.g. Ting & Kirby 1995; Petti & Longo 2001). The phase-averaged spatial spectrum provides greater insight into the turbulence structure, as the flow is phase dependent. Ensemble-averaged spectra were determined from the 200 instantaneous one-dimensional velocity spatial spectra of the instantaneous velocity field at a given elevation and phase.

3.1.1. Evolution of the integral length scale: evolving towards two-dimensional turbulence

The longitudinal integral length scale $\langle L_{11} \rangle$, defined as (Pope 2000)

$$\langle L_{11} \rangle = \frac{\pi \langle S_{uu}(\kappa_1 = 0) \rangle}{2 \langle u'^2 \rangle}, \quad (3.1)$$

was obtained from the one-dimensional longitudinal spatial spectra $\langle S_{uu} \rangle$ at the longitudinal wavenumber $\kappa_1 = 0$. Figure 6 shows the variations of $\langle L_{11} \rangle$ as well as its local phase-averaged water depth $\langle h(t) \rangle$ normalized value for each cross-shore location. The value of $\langle L_{11} \rangle / \langle h \rangle$ is typically 0.1–0.3, consistent with previous findings under broken waves (e.g. Pedersen, Deigaard & Sutherland 1998). Our results indicate that $\langle L_{11} \rangle / \langle h \rangle$ remains within the range 0.1–0.2 in the surf zone, but the ratio increases up to 0.4 in the swash zone (figure 6b). This indicates that in the swash zone the water depth decreases faster than the evolution time scale of $\langle L_{11} \rangle$, suggesting that the falling free surface may constrain the dimensionality of the turbulence to be less than three.

Shallow-water flow studies have demonstrated that vertical confinement can constrain the large-scale turbulence structure to horizontal motions, resulting in two-dimensional turbulence (Chen & Jirka 1995; Uijttewaalt & Booij 2000; Uijttewaalt &

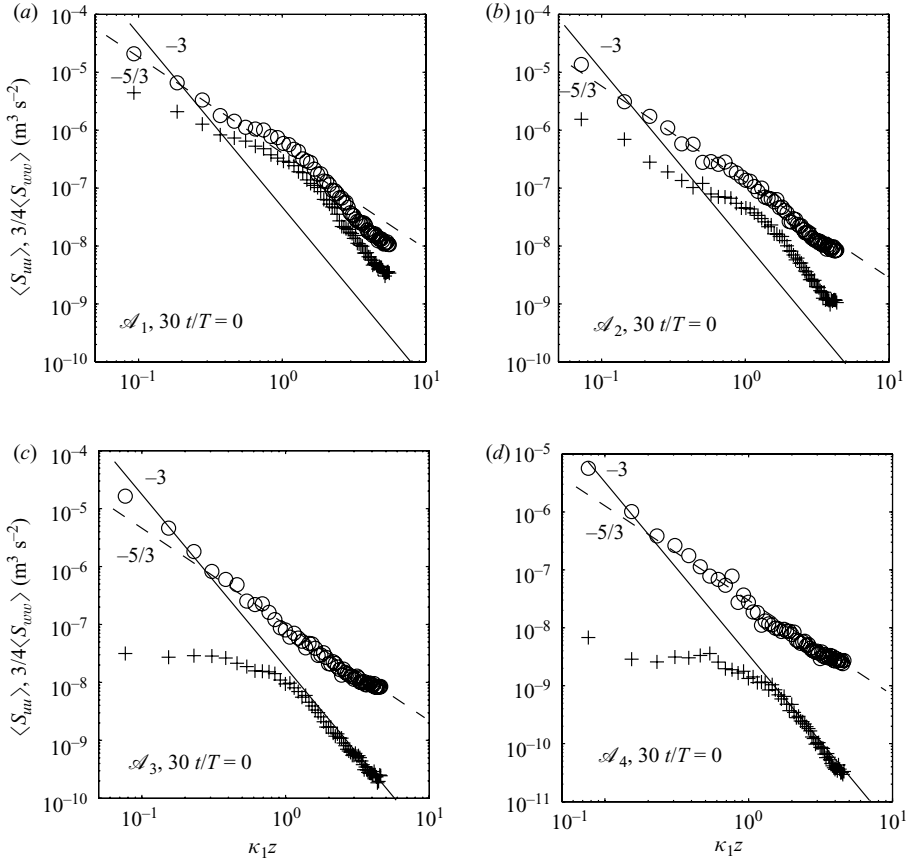


FIGURE 7. Spatial spectra $\langle S_{uu} \rangle$ and $(3/4)\langle S_{ww} \rangle$ within the water column at the bore-front phase $t/T=0$ at measurement locations (a) \mathcal{A}_1 , (b) \mathcal{A}_2 , (c) \mathcal{A}_3 and (d) \mathcal{A}_4 ; the wavenumber is non-dimensionalized with the elevation z of the spectra: \circ , $\langle S_{uu} \rangle$; $+$, $(3/4)\langle S_{ww} \rangle$; —, -3 slope; ---, $-5/3$ slope.

Jirka 2003) and a resultant inverse TKE cascade characterized by a -3 power law at larger scales of the one-dimensional energy spectrum (Kraichnan 1967; Davidson 2004). Uijttewaai & Jirka (2003), studying grid turbulence in shallow flows, found a -3 spectral slope at low frequencies (larger length scales relative to the water depth) and a -1 slope at moderate frequencies (length scales smaller than the water depth) which they attributed to boundary-modified three-dimensional turbulence structure.

In our study $\langle L_{11} \rangle / \langle h \rangle$ at $t/T=0$ for locations \mathcal{A}_1 , \mathcal{A}_2 , \mathcal{A}_3 and \mathcal{A}_4 is 0.34, 0.23, 0.40 and 0.59, respectively (figure 6b). Figure 7 shows both the longitudinal and the transverse spectra at mid-water depth at each cross-shore location. The energy level of the transverse spatial spectra is significantly smaller than the longitudinal spatial spectra in the inner surf zone \mathcal{A}_3 (figure 7c) and swash zone \mathcal{A}_4 (figure 7d). Plots of $\langle S_{ww} \rangle$ indicate that at all scales but particularly at low wavenumber ($\kappa_1 z < 0.5$), vertical fluctuation energy decreases increasingly rapidly as the swash zone is approached, being most pronounced in the swash zone (\mathcal{A}_4). This is suggestive of the rapidly decreasing water depth constraining the vertical turbulence motions. A characteristic -3 slope of two-dimensional turbulence becomes increasingly apparent as the shoreline is approached with a fairly clear -3 slope found at \mathcal{A}_4 (figure 7d).

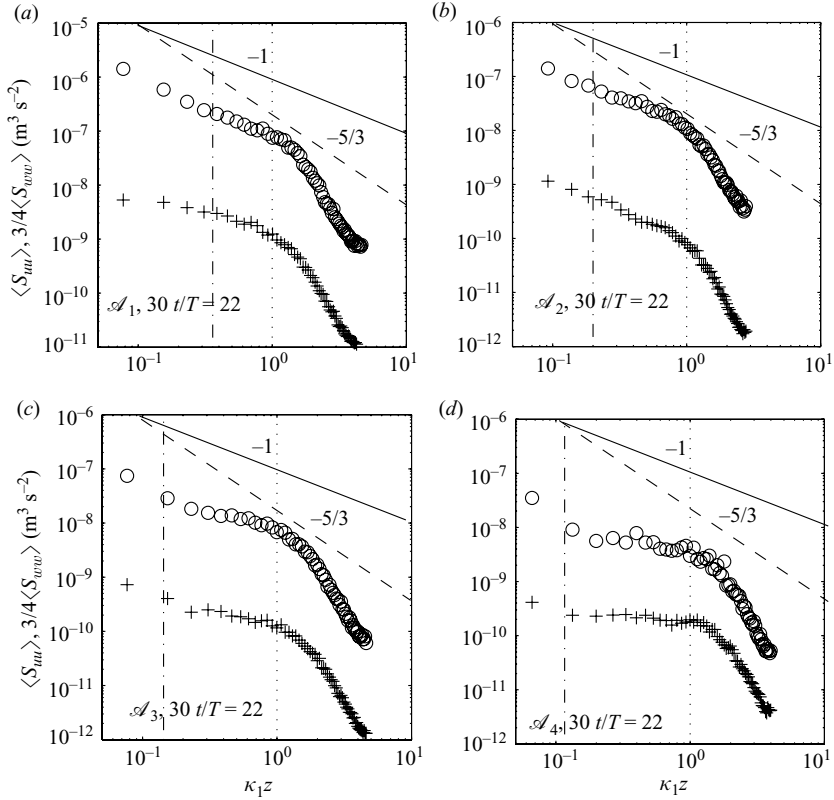


FIGURE 8. Spatial spectra $\langle S_{uu} \rangle$ and $(3/4)\langle S_{ww} \rangle$ near the bed during the downwash phase $30t/T = 22$ at measurement locations (a) \mathcal{A}_1 , (b) \mathcal{A}_2 , (c) \mathcal{A}_3 and (d) \mathcal{A}_4 ; the wavenumber is non-dimensionalized with the elevation z of the spectra: \circ , $\langle S_{uu} \rangle$; $+$, $(3/4)\langle S_{ww} \rangle$; ---, $-5/3$ slope; —, -1 slope; \cdots , $\kappa_1 z = 1$; $- \cdot - \cdot -$, $\kappa_1 z = z/\mathcal{H}$.

3.1.2. Bed-generated turbulence: the -1 spectral law

The energy injection from the bed-generated eddies (characteristic length scale of the order of the elevation z) modifies the slope of the energy cascade. Nikora (1999) demonstrated that a region of -1 slope in the energy cascade exists between the energy-containing range and the inertial subrange because of the superposition of the bed-generated eddies at all possible distances from the wall. In the inertial subrange, the one-dimensional energy spectrum is proportional to $\epsilon^{2/3} \kappa_1^{-5/3}$, in which ϵ is the turbulence dissipation rate. The increase in ϵ because of the energy injection from the bed-generated eddies with the characteristic scale z is of the order of u_*^3/z , in which u_* is the friction velocity. Hence, the superposition of the energy cascades modifies the slope of the inertial range from $-5/3$ to -1 as

$$\langle S_{uu}(\kappa_1) \rangle \sim \epsilon^{2/3} \kappa_1^{-5/3} \sim u_*^2 \kappa_1^{-1}. \quad (3.2)$$

Figure 8 shows the spatial spectra near the bed during the downwash phase ($30t/T = 22$) at each cross-shore location. The wavenumber κ_1 is non-dimensionalized by the elevation z of the spatial spectra; $\langle S_{uu} \rangle$ shows a slope of -1 at smaller wavenumbers (roughly $\kappa_1 z \leq 1$), consistent with the wall-bounded turbulence spectral model of Nikora (1999). It is predicted that the -1 slope region lies within the range $z/\mathcal{H} \leq \kappa_1 z \leq 1$, where \mathcal{H} is the characteristic length scale of the flow (i.e. the boundary

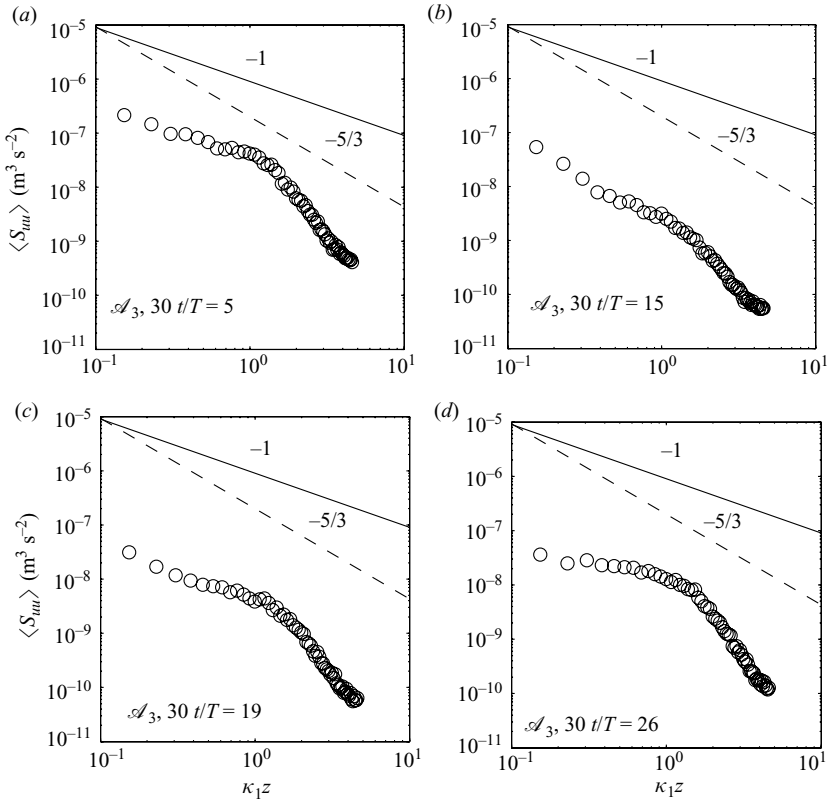


FIGURE 9. Spatial spectra $\langle S_{uu} \rangle$ near the bed at four phases, (a) $30t/T = 5$, (b) $30t/T = 15$, (c) $30t/T = 19$ and (d) $30t/T = 26$ at measurement location \mathcal{A}_3 ; the wavenumber is non-dimensionalized with the elevation z of the spectra.

layer thickness in our case). With the boundary layer thickness directly calculated from the phase-averaged velocity field at $30t/T = 22$ at each cross-shore location, the values of z/\mathcal{H} are 0.362, 0.200, 0.143 and 0.116 for \mathcal{A}_1 , \mathcal{A}_2 , \mathcal{A}_3 and \mathcal{A}_4 , respectively (figure 8).

Furthermore, our measurements (figure 9) suggest that during the uprush phase the superposition of bore-generated turbulence and the offshore smaller-scale turbulent energy generated at the bed yields the characteristic -1 slope at the measurement location at wavenumbers in the region $\kappa_1 z \leq 1$ (figure 9a). As phase advances, the slope relaxes to $-5/3$, as the offshore bed-generated smaller-scale turbulence has decayed (figure 9b). Eventually, the -1 slope appears again during the downwash phases because of the energy injection from the bed when the boundary layer is developing (figures 9c and 9d). In the surf zone, there is a relatively small amount of energy injection from the bed-generated turbulence during the latter part of the uprush phase, that is to say the reversal phases, and the early part of the downwash phases. For the swash zone, the -1 slope is apparent even during the latter part of the uprush phase, the reversal phases, which reconfirms that the bed-generated turbulence is important in the swash zone.

3.2. Evolution of the turbulent kinetic energy

The TKE k is defined as

$$k = \frac{1}{2} \langle u'_i u'_i \rangle, \quad (3.3)$$

and its evolution equation is (Pope 2000)

$$\frac{\partial k}{\partial t} + \langle u \rangle \cdot \nabla k = -\nabla \cdot T' + \mathcal{P} - \epsilon, \quad (3.4)$$

where \mathcal{P} is the production of TKE and T' is defined as

$$T' = \frac{1}{2} \langle u'_i u'_j u'_j \rangle + \frac{\langle u'_i p' \rangle}{\rho} - 2\nu \langle u'_j s_{ij} \rangle, \quad (3.5)$$

in which p' is the pressure fluctuation, ρ the density and s_{ij} the fluctuating rate of strain tensor, defined as

$$s_{ij} = \frac{1}{2} \left(\frac{\partial u'_i}{\partial x_j} + \frac{\partial u'_j}{\partial x_i} \right). \quad (3.6)$$

Further, \mathcal{P} and ϵ are defined as

$$\mathcal{P} = -\langle u'_i u'_j \rangle \frac{\partial \langle u_i \rangle}{\partial x_j} \quad (3.7)$$

and

$$\epsilon = 2\nu \langle s_{ij} s_{ij} \rangle. \quad (3.8)$$

The evolution equation for k shows that the local time rate of the change of TKE is due to convection by the mean flow, diffusive transport by the pressure and turbulent fluctuations, production and dissipation.

Given our two-dimensional measurements, TKE is estimated as

$$k = \frac{1.33}{2} \left(\langle u'^2 \rangle + \langle w'^2 \rangle \right) \quad (3.9)$$

following Ting & Kirby (1995) and Chang & Liu (1999). The value of 1.33 is based on the assumption that breaking waves have characteristics similar to plane wakes, in which the ratio of $\langle u'^2 \rangle$ and $\langle w'^2 \rangle$ is 1.31 (Svendsen 1987). Our results indicate that the average ratio $\langle u'^2 \rangle / \langle w'^2 \rangle$ is 1.36. The ratio is as high as 10 when it is close to the bed, which is expected because the bed constrains the vertical fluctuations.

The relative importance of bore-generated, advected and bed-generated turbulence can be investigated by comparing the TKE at the initial bore-front phases to that at the latter part of the downwash phases. Figures 10 and 11 show the TKE at the bore-front phases and the downwash phases, respectively, at all cross-shore locations. The TKE is non-dimensionalized by the global maximum TKE ($0.0251 \text{ m}^2 \text{ s}^{-2}$) at $30t/T = 2$ at cross-shore location \mathcal{A}_1 .

The breaking-wave- and bore-generated turbulence are the main sources of turbulent energy. The breaking wave crest plunges into the water approximately 10 cm offshore of location \mathcal{A}_1 ; then the bore propagates across measurement locations \mathcal{A}_1 – \mathcal{A}_4 . The first phase of each location does not necessarily have the maximum turbulence intensity, since it takes time for the bore turbulence to advect into the measurement area. The measured global maximum TKE occurs just after the wave plunges into the water, i.e. at \mathcal{A}_1 . At the bore-front phases ($30t/T = 0$ and 1), a strong TKE level is apparent over the majority of the water column at locations \mathcal{A}_1 and \mathcal{A}_2

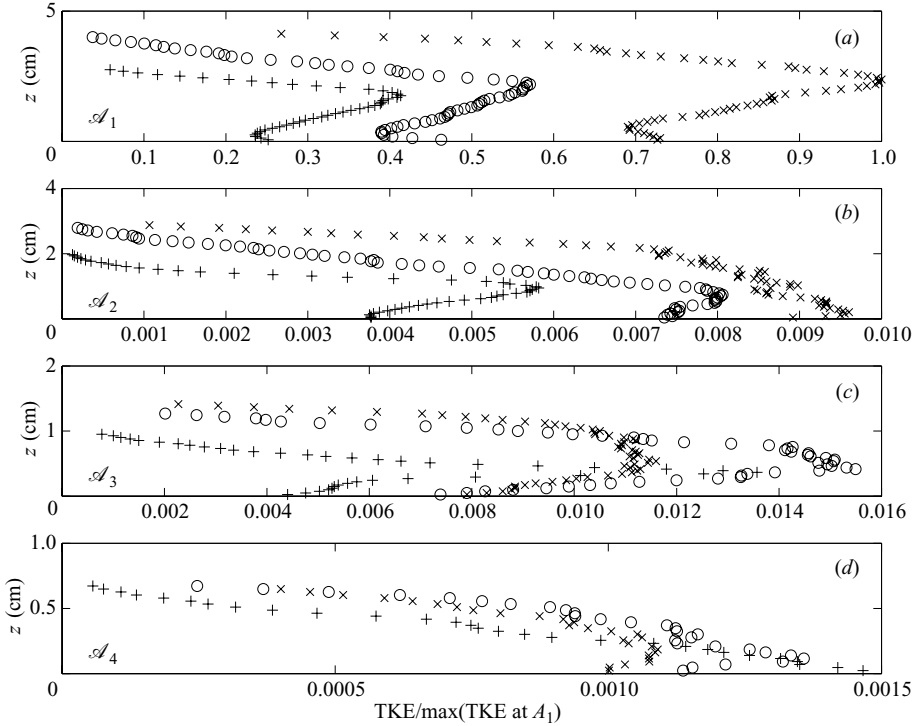


FIGURE 10. Vertical profile of the non-dimensionalized TKE $k(t)/\max(k(30t/T=2))$ averaged across the FOV at the bore-front phases at measurement locations (a) \mathcal{A}_1 , (b) \mathcal{A}_2 , (c) \mathcal{A}_3 and (d) \mathcal{A}_4 : +, $t/T=0$; O, $30t/T=1$; X, $30t/T=2$.

(figures 10a and 10b). A strong shear-layer-generated TKE peak is apparent roughly at mid-water column (because of the interaction between the downwash and uprush flows). The shear-layer-generated TKE is relatively strong at \mathcal{A}_3 (figure 10c), as the velocity gradient $\partial\langle u\rangle/\partial z$ is large (see figure 5).

The TKE decays rapidly from \mathcal{A}_1 to \mathcal{A}_4 (figures 10a–10d). The bore-generated and advected TKE are dominant during the early uprush phases for the cross-shore locations \mathcal{A}_1 , \mathcal{A}_2 and \mathcal{A}_3 . A discussion of bore-generated versus advected TKE requires a discussion of \mathcal{P} and will be deferred to § 3.2.1.

The TKE results indicate that in the outer surf zone (\mathcal{A}_1 and \mathcal{A}_2), the bed-generated turbulence contributes minimally to total TKE even during the downwash phases, as the advected TKE level is still quite high in the water column (figures 11a and 11b). This balance changes in the inner surf (\mathcal{A}_3) and swash (\mathcal{A}_4) zones, where the near-bed TKE is higher than that in the water column during the latter part of the downwash phase (figures 11c and 11d). The balance shifts, since the advected TKE has decayed significantly, and the longer duration of the downwash phase allows time for the bed-generated turbulence to grow. Thus, the bed-generated turbulence is dominant during the downwash phase in the inner surf and swash zones.

3.2.1. TKE production: shear-layer-generated turbulence in the surf zone

TKE production is estimated from the measured two-dimensional flow fields based on (3.7). As only the terms in the x – z plane are available, \mathcal{P} is estimated from the

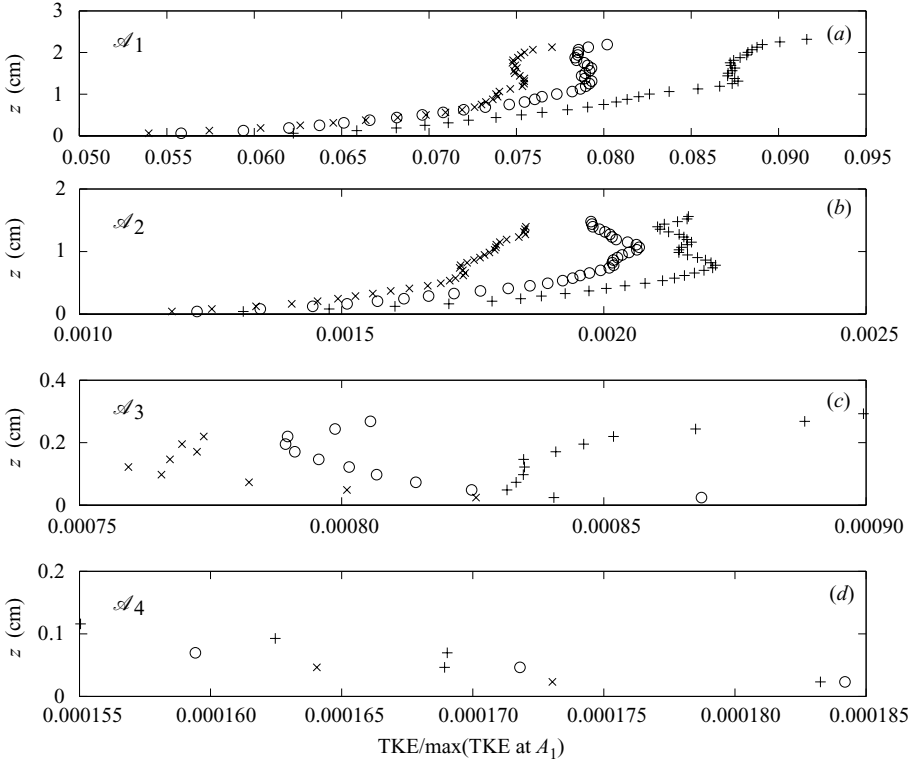


FIGURE 11. Vertical profile of the non-dimensionalized TKE $k(t)/\max(k(30t/T=2))$ at \mathcal{A}_1 at the downwash phases at measurement locations (a) \mathcal{A}_1 , (b) \mathcal{A}_2 , (c) \mathcal{A}_3 and (d) \mathcal{A}_4 : +, $30t/T=25$; O, $30t/T=26$; x, $30t/T=27$.

PIV data as

$$\mathcal{P} = -\langle u'w' \rangle \frac{\partial \langle u \rangle}{\partial z} - \langle u'w' \rangle \frac{\partial \langle w \rangle}{\partial x} - \langle u'u' \rangle \frac{\partial \langle u \rangle}{\partial x} - \langle w'w' \rangle \frac{\partial \langle w \rangle}{\partial z}. \quad (3.10)$$

The sign of \mathcal{P} is sensitive to the sign of the velocity gradients, which are contaminated with local (higher-spatial-frequency) noise because of their determination by central differencing. The phase-averaged velocity field is quite homogeneous in the streamwise direction within the measurement area except at the bore-front phases, the reverse phase and the last downwash phase. In order to reduce the noise induced by the differencing of the velocity fields, the phase-averaged velocity was smoothed in the x direction. A second-order polynomial function was fit to the velocity data in a least squares sense at each z elevation. A scaling analysis of (3.10) suggests that $\partial \langle u \rangle / \partial x \ll \partial \langle u \rangle / \partial z$, basically a boundary layer assumption, and as the flow is dominantly bed parallel, $\partial \langle w \rangle / \partial z \ll \partial \langle w \rangle / \partial x$. On this basis, the last two terms in (3.10) are neglected yielding a more robust estimate of \mathcal{P} ; thus, the production is estimated as

$$\mathcal{P} = -\langle u'w' \rangle \frac{\partial \langle u \rangle}{\partial z} - \langle u'w' \rangle \frac{\partial \langle w \rangle}{\partial x}. \quad (3.11)$$

Figure 12 shows the \mathcal{P} estimates obtained from both (3.10) and (3.11) and from their percentage difference at the bore-front phase $t/T=0$ at \mathcal{A}_3 . The highest percentage

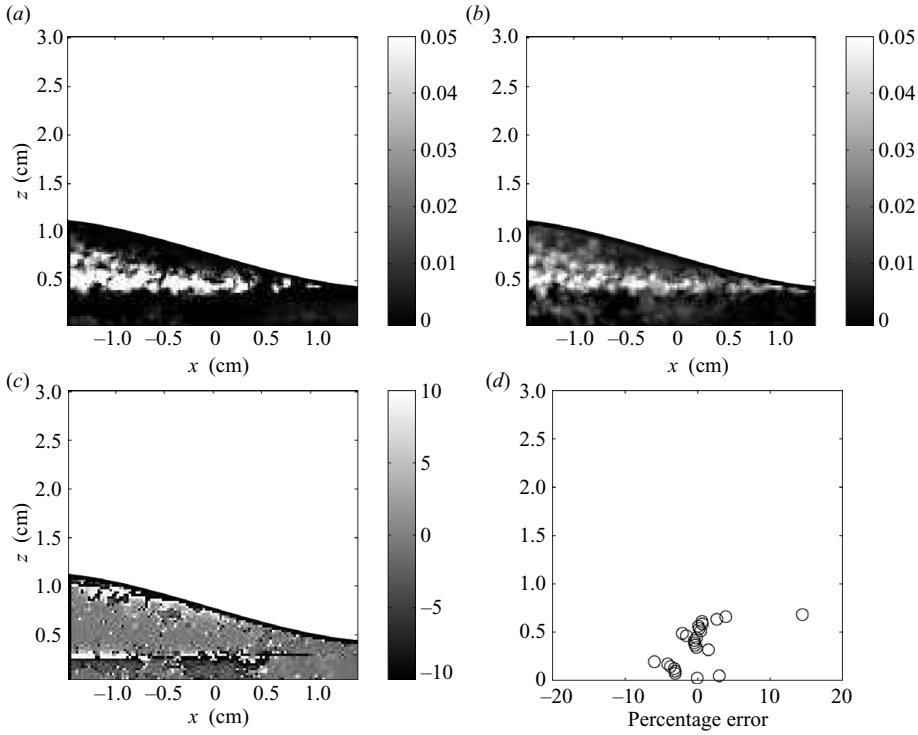


FIGURE 12. Uncertainty of \mathcal{P} estimates during the uprush bore front $t/T=0$ at \mathcal{A}_3 ; (a) \mathcal{P} ($\text{m}^2 \text{s}^{-3}$) estimated from (3.11); (b) \mathcal{P} ($\text{m}^2 \text{s}^{-3}$) estimated from (3.10); (c) percentage difference between \mathcal{P} from 3.11 and 3.10; (d) the vertical profile of the percentage difference of the \mathcal{P} estimates.

difference is 16% which occurs near the free surface. High percentage differences also occur close to the bed.

Figure 13 shows the vertical profile of \mathcal{P} and TKE, horizontally averaged across the FOV, at the bore-front phases at cross-shore locations \mathcal{A}_1 , \mathcal{A}_2 and \mathcal{A}_3 . The importance of shear-layer-generated \mathcal{P} is seen at cross-shore location \mathcal{A}_3 . The strong \mathcal{P} is due to the steep velocity gradient between $z=0.3$ cm and $z=0.6$ cm; \mathcal{P} at each cross-shore location is non-dimensionalized by the maximum value of \mathcal{P} at $t/T=0$ at location \mathcal{A}_3 . Similarly, TKE is non-dimensionalized by its maximum value at $t/T=0$ at the same location.

Figure 13 indicates that \mathcal{P} is at its global maximum in the shear layer at cross-shore location \mathcal{A}_3 . The local maximum \mathcal{P} at \mathcal{A}_1 and \mathcal{A}_2 is roughly 0.15 ($30t/T=0$ and 1 in figure 13); thus, the maximum \mathcal{P} generated by the shear layer at \mathcal{A}_3 is 6.7 times greater than that at \mathcal{A}_1 and \mathcal{A}_2 . The measurements indicate that the normalized TKE decays from 0.78 to 0.42 between locations \mathcal{A}_1 and \mathcal{A}_2 . If the TKE is solely the bore-advected TKE, then the normalized level that arrives at location \mathcal{A}_3 should be less than 0.42. Figure 13 shows that the level has instead increased to greater than 1, indicating that the shear-layer-generated \mathcal{P} has significantly augmented the turbulence level at $30t/T=1$ at \mathcal{A}_3 . This result indicates that the shear-layer-generated TKE at \mathcal{A}_3 is significantly stronger than at either \mathcal{A}_1 or \mathcal{A}_2 ; i.e. the shear layer in the inner surf zone generates more TKE compared with the outer surf zone.

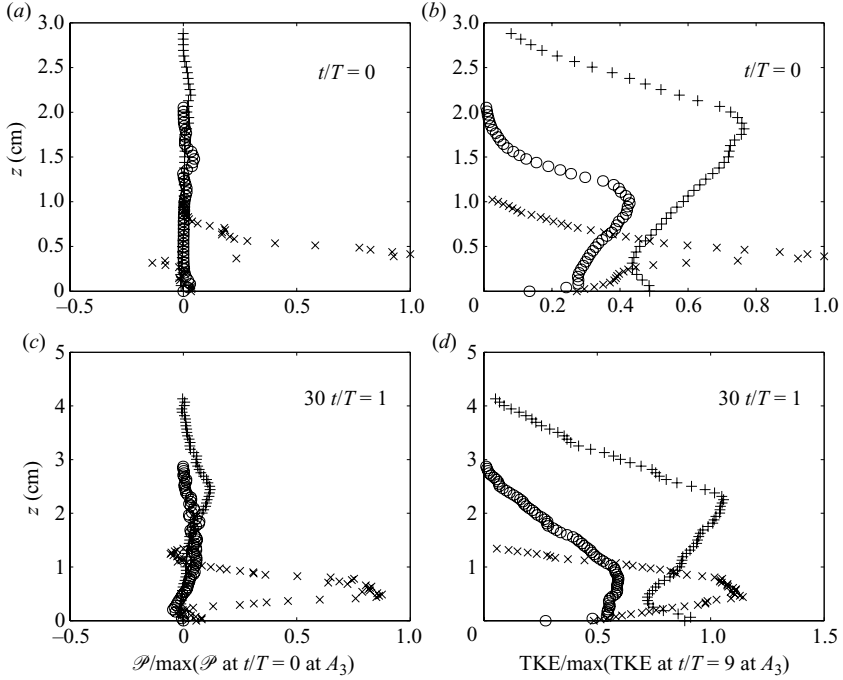


FIGURE 13. (a) Vertical profiles of $\mathcal{P}(t)/\max(\mathcal{P}(30t/T=0 \text{ at } \mathcal{A}_3))$ at the phase $30t/T=0$, (b) vertical profiles of $k(t)/\max(k(30t/T=0 \text{ at } \mathcal{A}_3))$ at the phase $30t/T=0$, (c) vertical profiles of $\mathcal{P}(t)/\max(\mathcal{P}(30t/T=0 \text{ at } \mathcal{A}_3))$ at the phase $30t/T=1$ and (d) vertical profiles of $k(t)/\max(k(30t/T=0 \text{ at } \mathcal{A}_3))$ at the phase $30t/T=1$ at measurement locations \mathcal{A}_1 , \mathcal{A}_2 , and \mathcal{A}_3 : +, \mathcal{A}_1 ; \circ , \mathcal{A}_2 ; \times , \mathcal{A}_3 .

3.2.2. Turbulent dissipation: turbulence decay during the latter part of uprush and the early part of downwash

The PIV-measured turbulent fluctuation gradients were used to estimate the turbulent dissipation directly. Since only the horizontal and vertical gradients were measured, not all the terms in the dissipation are available from the measurements. The dissipation ϵ was estimated as follows Doron *et al.* (2001):

$$\epsilon = \nu \left[4 \left\langle \left(\frac{\partial u'}{\partial x} \right)^2 \right\rangle + 4 \left\langle \left(\frac{\partial w'}{\partial z} \right)^2 \right\rangle + 3 \left\langle \left(\frac{\partial u'}{\partial z} \right)^2 \right\rangle + 3 \left\langle \left(\frac{\partial w'}{\partial x} \right)^2 \right\rangle + 6 \left\langle \left(\frac{\partial u'}{\partial z} \frac{\partial w'}{\partial x} \right) \right\rangle + 4 \left\langle \left(\frac{\partial u'}{\partial x} \frac{\partial w'}{\partial z} \right) \right\rangle \right]. \quad (3.12)$$

All gradients were estimated by a central difference. Cowen & Monismith (1997) argued that the length scale of this difference should be approximately 5. If it is too small, significant error is introduced because of the amplification of noise; if it is too large, the gradients are under-resolved and the dissipation is underestimated. The time-averaged Kolmogorov length scale $\eta = (\nu^3/\epsilon)^{1/4}$ is found to be 0.17 mm, 0.15 mm, 0.14 mm and 0.17 mm for measurement locations \mathcal{A}_1 , \mathcal{A}_2 , \mathcal{A}_3 and \mathcal{A}_4 , respectively. Hence, the central difference length scale lies in the range 3η – 7η at the four locations, consistent with the suggestion of Cowen & Monismith (1997).

Our results indicated that ϵ is of the order of $0.02 \text{ m}^2 \text{ s}^{-3}$ at \mathcal{A}_1 and \mathcal{A}_2 (outer surf zone) and increases to as high as $0.1 \text{ m}^2 \text{ s}^{-3}$ at \mathcal{A}_3 , where the shear layer occurs. This result is consistent with the field study of Cox, Hobensack & Sukumaran (1994), which indicated that ϵ increased towards the shore in the surf zone. Raubenheimer, Elgar & Guza (2004), analysing field data, found ϵ to be of the order of $0.04 \text{ m}^2 \text{ s}^{-3}$ in the inner surf zone and $0.1 \text{ m}^2 \text{ s}^{-3}$ in the swash zone. Contrary to the *in situ* results of Raubenheimer *et al.* (2004), our measured dissipation rate decreases from the inner surf zone to of the order of $0.01 \text{ m}^2 \text{ s}^{-3}$ near the bed in the swash zone (\mathcal{A}_4). This discrepancy may result from several causes including roughness and permeability effects, scale effects, the idealized monochromatic swash zone in the laboratory compared with the time-varying swash zone in the field and the challenges of extracting dissipation from field measurements from a non-periodic swash zone (which would lead to enhanced estimates of dissipation because of overestimates of the perturbation velocity field). In addition, our results find that the production is insignificant in the swash zone; hence, less TKE is available to dissipate in the swash zone in comparison with the inner surf zone in which the production and dissipation are roughly in balance at the shear layer.

The present results, consistent with our previous study for both plunging and spilling breakers in the swash zone (Cowen *et al.* 2003), suggest that the temporal decay rates of TKE and ϵ are equivalent to that expected for grid turbulence (Pope 2000). Both TKE and ϵ decay as power laws with the decay exponents 1.3 and 2.3 for the TKE and ϵ , respectively. The detailed discussion can be found in Cowen *et al.* (2003). The results suggest that during the deceleration phases, the reversal phases and the early downwash phases, there is no significant mean shear in the water column ($\mathcal{P} \simeq 0$) and the boundary layer does not significantly affect the flow; thus the turbulence evolves as free turbulence without boundaries.

3.2.3. *Production and dissipation: local equilibrium of turbulence*

Some studies in the surf and swash zones (Cox, Hobensack & Sukumaran 2000; Puleo & Holland 2001; Raubenheimer *et al.* 2004) estimate friction coefficients with the assumption of a local equilibrium of turbulence ($\mathcal{P} \simeq \epsilon$) near the bed, which is known to hold in the wall region of turbulent boundary layers (Tennekes & Lumley 1972; Pope 2000). Raubenheimer *et al.* (2004) also estimated friction coefficients by assuming that dissipation is balanced by the sum of production by near-bed shear layer and by wave breaking. In this section, the balance of the production and dissipation is examined.

Figures 14 and 15 show the horizontally averaged vertical profile of \mathcal{P} and ϵ at the bore-front and the downwash phases at each cross-shore location. The results show that once the bore front passes a given cross-shore location, \mathcal{P} decreases rapidly, becoming extremely small at the downwash phases; \mathcal{P} is less than ϵ at most of the phases, which indicates that the breaking-wave- and bore-front-generated turbulence is the major source of TKE in the surf zone. At location \mathcal{A}_1 , \mathcal{P} and ϵ are roughly in balance in the water column at $30t/T = 1$, as they are in the shear layer at location \mathcal{A}_3 ($30t/T = 0$) as indicated in figure 14, the latter being the expected result for free shear flows (Pope 2000). Bed-generated \mathcal{P} increases at the bed during the downwash phases, eventually becoming in balance with ϵ at the latter stage of the downwash at locations \mathcal{A}_1 and \mathcal{A}_2 (figures 15a and 15b); \mathcal{P} is small in the water column compared with ϵ during the downwash phases at all locations. In the inner surf zone \mathcal{A}_3 and the swash zone \mathcal{A}_4 , \mathcal{P} and ϵ at the bed never achieve a local equilibrium, even at the latter part of the downwash phase (figures 15c and 15d). We believe near-bed

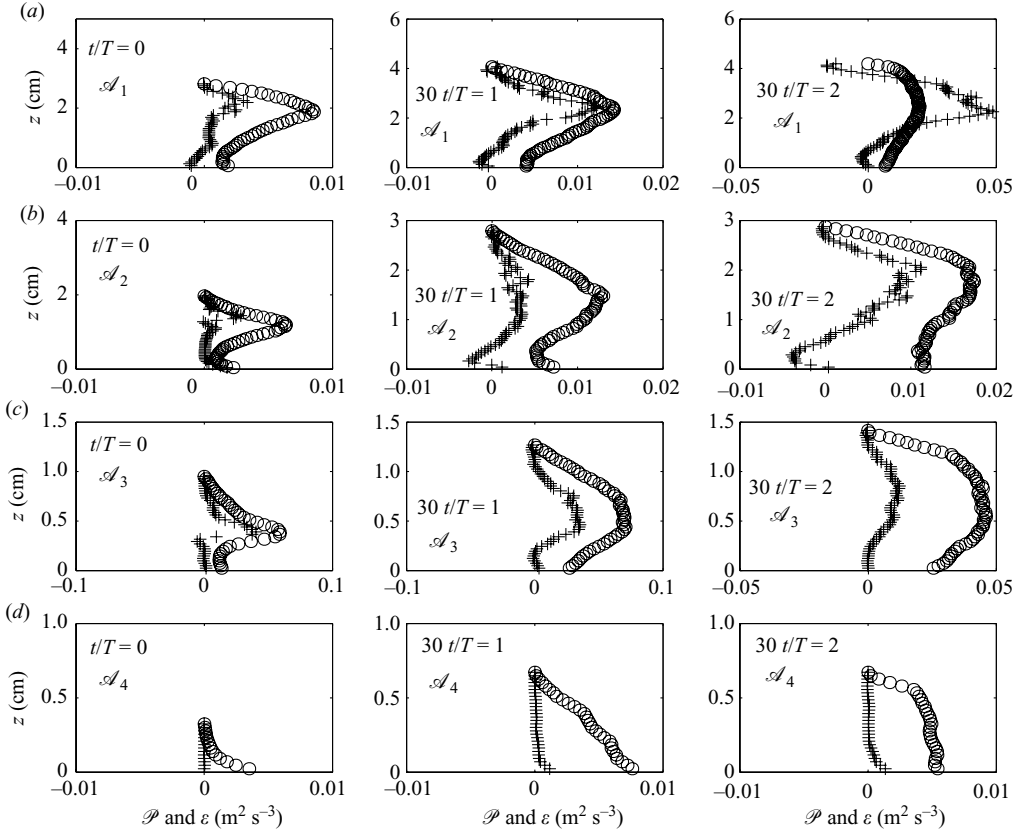


FIGURE 14. Vertical profiles of \mathcal{P} and ϵ at the bore-front phases $30t/T = 0$ to 2 at (a) \mathcal{A}_1 , (b) \mathcal{A}_2 , (c) \mathcal{A}_3 and (d) \mathcal{A}_4 : +, \mathcal{P} ; o, ϵ .

\mathcal{P} could increase and exceed ϵ during the downwash as the boundary layer grows if the time scale of the downwash is sufficiently long, as \mathcal{P} is expected to exceed ϵ in a growing boundary layer.

3.2.4. Turbulent kinetic energy budget

The evolution of TKE, which is governed by (3.4), is examined to gain insight into the TKE transport processes from the surf to the swash zones. The viscous transport can be neglected at a large Reynolds number. With the instantaneous free-surface measurements from the raw PIV images, the phase-averaged and instantaneous pressure fields ($\langle p \rangle$ and p) can be evaluated by depth-integrating the vertical momentum equation. Neglecting the shear stress terms, the phase-averaged and instantaneous pressure fields are expressed as (Mei 1989)

$$\langle p \rangle|_z = \rho g_z (\langle \zeta \rangle - z) + \rho \frac{\partial}{\partial t} \int_z^{\langle \zeta \rangle} \langle w \rangle dz + \rho \frac{\partial}{\partial x} \int_z^{\langle \zeta \rangle} \langle u \rangle \langle w \rangle dz - \rho \langle w \rangle^2|_z, \quad (3.13)$$

$$p|_z = \rho g_z (\zeta - z) + \rho \frac{\partial}{\partial t} \int_z^{\zeta} w dz + \rho \frac{\partial}{\partial x} \int_z^{\zeta} uw dz - \rho w^2|_z. \quad (3.14)$$

The pressure transport was found by estimating $p' = p - \langle p \rangle$ using (3.13) and (3.14). The highest pressure transport occurs at the bore-front phase which is of the order of

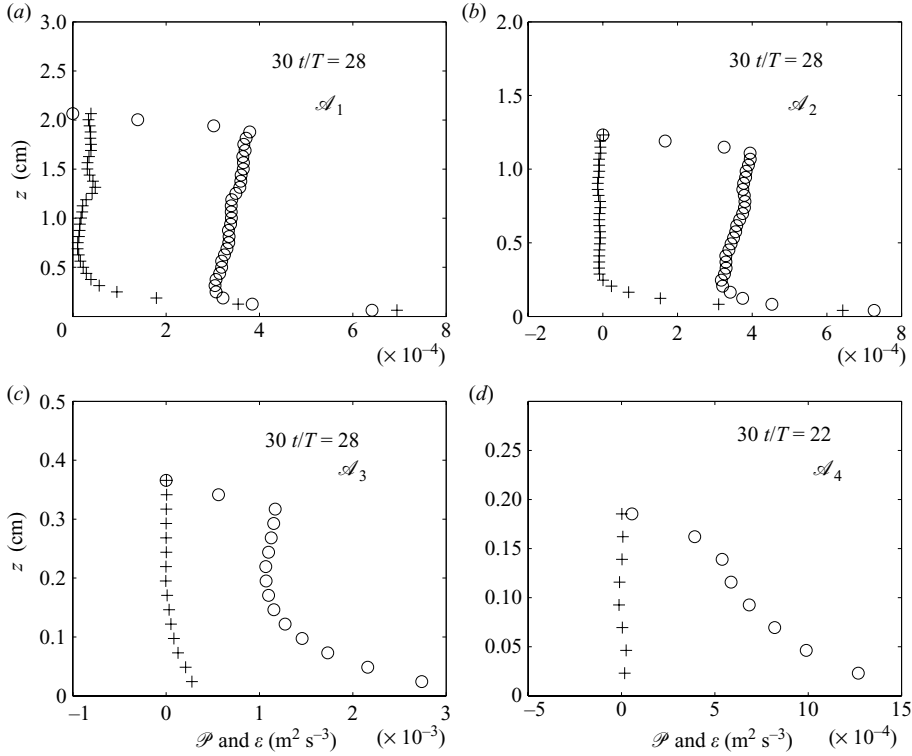


FIGURE 15. Vertical profiles of \mathcal{P} and ϵ during the downwash phase at (a) \mathcal{A}_1 , (b) \mathcal{A}_2 , (c) \mathcal{A}_3 and (d) \mathcal{A}_4 : +, \mathcal{P} ; o, ϵ .

$10^{-4} \text{ m}^2 \text{ s}^{-3}$. This is very small relative to the other terms in (3.4); hence, the pressure transport is neglected.

The overall temporal changes of the TKE can be examined by depth-integrating (3.4) from the bed $z = 0$ to the phase-averaged free surface $\langle \zeta \rangle$, yielding

$$\frac{\partial}{\partial t} k + A + T_t = P - D, \quad (3.15)$$

where k , A , T_t , P and D represent the depth-integrated TKE, advection, turbulent transport, production and dissipation, respectively. The depth-integral is not exactly along the gravitationally vertical axis, as the z direction is perpendicular to the beach face, which has a $1/20$ slope. The rotation-induced error is minor, as the cosine error is only 0.1% at a $1/20$ slope.

The individual terms $\partial k/\partial t$, A , T_t , P and $-D$ are shown in figure 16. Consistent with what has been discussed above at the latter part of the uprush phase and the early part of the downwash phase at locations \mathcal{A}_2 and \mathcal{A}_3 , the behaviour of the turbulence is similar to that of grid turbulence, which is balanced roughly as

$$\frac{\partial}{\partial t} k = -D. \quad (3.16)$$

The production is maximum in the first few phases ($t/T = 0-0.3$). Once the production becomes relatively small, $\partial k/\partial t$ becomes negative. The dissipation is at a local maximum when the production is at a local maximum. At location \mathcal{A}_1 , P is roughly in balance with D , while at locations \mathcal{A}_2 and \mathcal{A}_3 , P is smaller than D ; P becomes

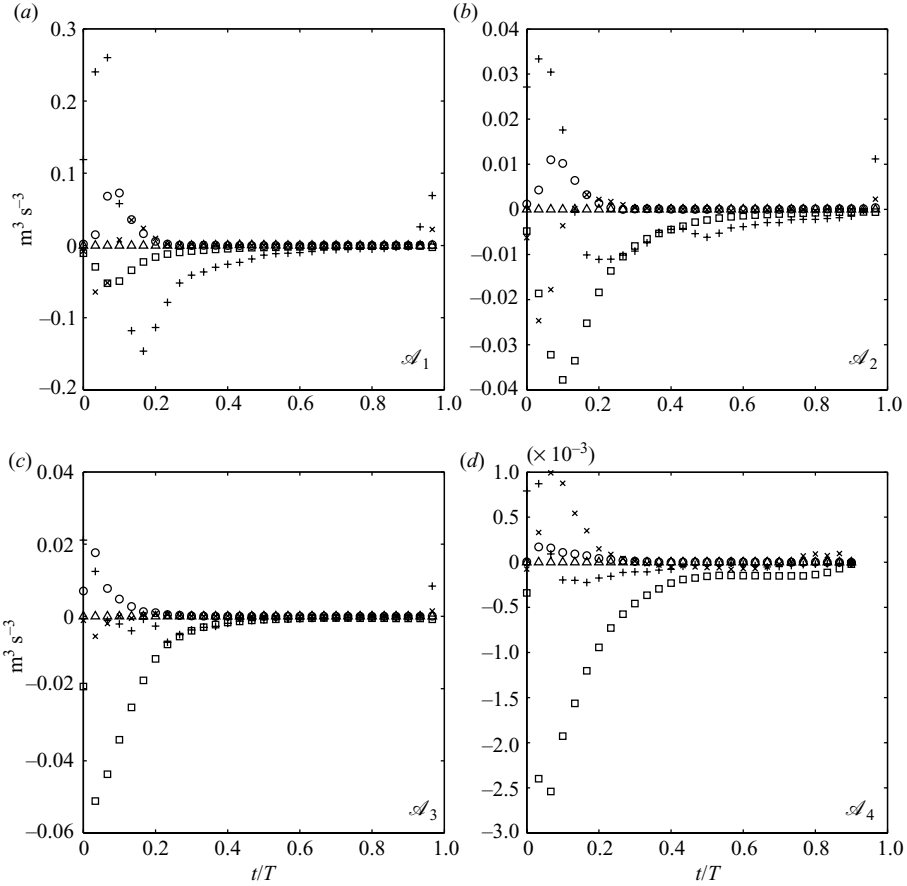


FIGURE 16. Depth-integrated TKE evolution at measurement locations (a) \mathcal{A}_1 , (b) \mathcal{A}_2 , (c) \mathcal{A}_3 and (d) \mathcal{A}_4 : +, $\partial k/\partial t$; \times , A ; \triangle , T_i ; \circ , P ; \square , $-D$.

insignificant at location \mathcal{A}_4 ; A is strong at phases at which the bore passes through the measurement area ($t/T \approx 0-0.3$). This is expected, as the advection is due to the strong horizontal gradient in TKE across the bore front. When the TKE is fairly homogeneous in the streamwise direction and the mean flow is primarily in the streamwise direction ($t/T > 0.3$), A is relatively small. It is apparent that $\partial k/\partial t$ is positive when A is negative and vice versa at locations \mathcal{A}_1 , \mathcal{A}_2 and \mathcal{A}_3 (figure 16). This is because the bore-generated turbulence is moving from offshore to onshore with the mean flow during the bore-front phases. When the bore-generated turbulence is moving within the measurement location, inhomogeneity of the TKE at the measurement location yields a negative A initially ($t/T < 0.1$) at surf zone locations \mathcal{A}_1 , \mathcal{A}_2 and \mathcal{A}_3 . This indicates that more TKE is moving into the measurement location than out of it at a particular phase, as $\partial k/\partial t$ is positive (k at the current phase is larger than that at the previous phase). Eventually, the bulk of bore-generated turbulence is moving out of the measurement location ($t/T > 0.1$), indicated by the negative $\partial k/\partial t$; A becomes positive, indicating that more TKE moves out of the measurement location than into it. In the swash zone \mathcal{A}_4 , A is always positive during the bore-front phases. This is because the bore-generated turbulence decays

significantly in the swash zone and the TKE is relatively uniform in the streamwise direction.

Another way to examine temporal changes in the overall depth-integrated TKE budget is by integrating (3.15) with respect to time. The time integration of the depth-integrated equation (3.15) can be written as

$$K + [A] + [T_t] = [P] - [D], \tag{3.17}$$

in which

$$K = k(t) - k(t = 0), \tag{3.18}$$

$$[A](t) = \int_0^t \int_0^{\langle \zeta \rangle} \left(\langle u \rangle \frac{\partial k}{\partial x} + \langle w \rangle \frac{\partial k}{\partial z} \right) dz dt, \tag{3.19}$$

$$[T_t](t) = \int_0^t \int_0^{\langle \zeta \rangle} \left(\frac{\partial}{\partial x} \langle u'k \rangle + \frac{\partial}{\partial z} \langle w'k \rangle \right) dz dt, \tag{3.20}$$

$$[P](t) = \int_0^t \int_0^{\langle \zeta \rangle} \mathcal{P} dz dt, \tag{3.21}$$

$$[D](t) = \int_0^t \int_0^{\langle \zeta \rangle} \epsilon dz dt. \tag{3.22}$$

The temporal changes of the terms in (3.17) are shown in figure 17. At all cross-shore locations, the magnitude of the local K is at its highest when $[P]$ becomes constant (constant $[P]$ between two phases indicates no additional TKE production as phase advances because $[P]$ is the temporal production increment). Thus, K decreases throughout the phases at which $[P]$ remains constant. This indicates that the TKE cannot maintain itself when TKE production is small; $[T_t]$ which does not exceed $8 \times 10^{-4} \text{ m}^2 \text{ s}^{-3}$ is relatively insignificant compared with the other terms at all locations. This is reasonable, especially after the bore-front phase when the turbulence is quite homogeneous in the streamwise direction, as the transport term should be zero for homogeneous turbulence. Further, $[D]$ follows the trend of $[P]$: when $[P]$ becomes constant, $[D]$ increases very slowly, indicating that the dissipation rate is decreasing with phase as the production rate decreases, which should be the case, as less energy cascades from the large-scale turbulence to the small scales. At location \mathcal{A}_1 , $[P]$ and $[D]$ are about the same at $t/T = 0-0.2$; $[D]$ is slightly higher than $[P]$ starting from $t/T > 0.2$. At location \mathcal{A}_4 , the magnitudes of K and $[P]$ are relatively small. The dissipation is dominant in the swash zone.

It is clear that the TKE budget is not in equilibrium locally at each cross-shore location. When integrating over the flow from the breaker line to the shoreline, the sum of the advection and transport terms yields zero, as these terms are simply the transfer of the TKE from place to place and cannot change the overall TKE. Therefore, the increase or decrease in TKE is due to the difference between the production and dissipation globally. Based on the overall evolution of the TKE budget from the offshore location \mathcal{A}_1 to the onshore location \mathcal{A}_4 , the TKE budget should be in equilibrium from the breaker line to the swash zone. It is apparent that the production exceeds the dissipation at location \mathcal{A}_1 at the bore-front phases ($30t/T = 2$ and 3). It is believed that the production is dominant at the locations offshore of \mathcal{A}_1 , where the wave plunges into the free surface. The dissipation is dominant in the inner surf and swash zones, and the swash zone is mainly a dissipater.

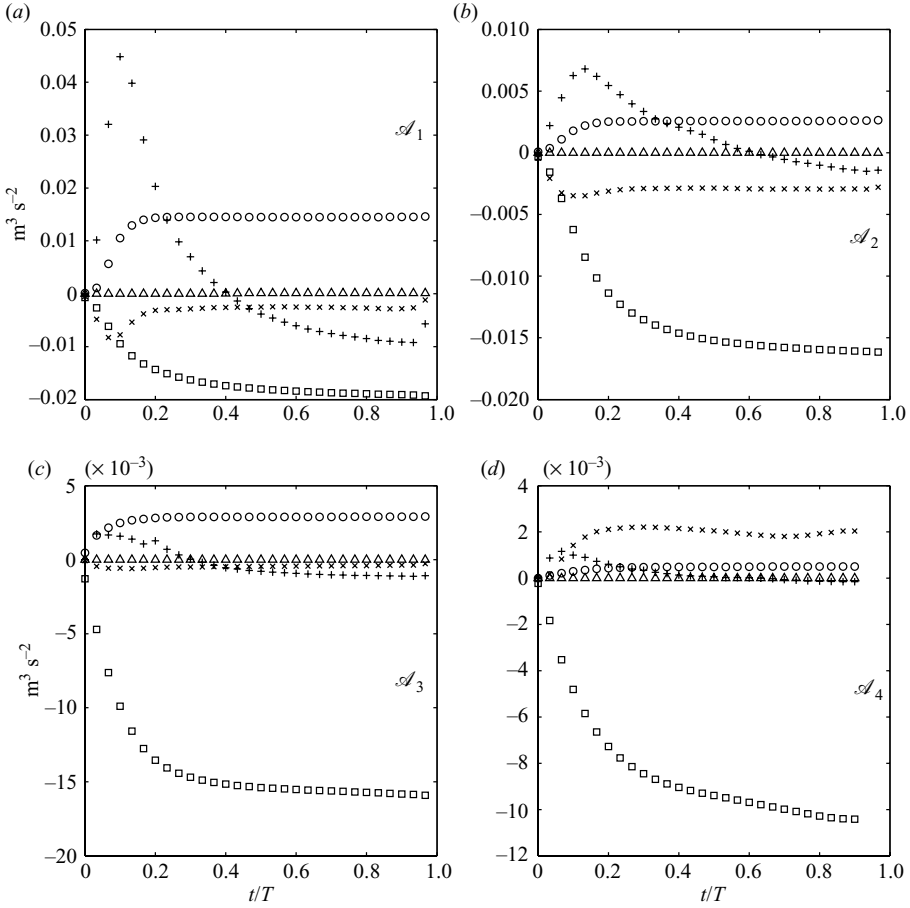


FIGURE 17. The evolution of the depth-integrated TKE budget components at measurement locations (a) \mathcal{A}_1 , (b) \mathcal{A}_2 , (c) \mathcal{A}_3 and (d) \mathcal{A}_4 : +, K ; \times , $[A]$; \triangle , $[T_f]$; \circ , $[P]$; \square , $-[D]$.

4. Conclusions

The phase-dependent vertically resolved flow fields within laboratory-modelled surf and swash zones were examined using a PIV measurement technique. The temporal evolution of the turbulence can be divided into three intervals over a wave cycle: (i) the wave-breaking-generated turbulence and the shear-layer-generated turbulence at the bore-front phases at which the large-scale turbulence is generated; (ii) a decay stage, analogous to grid turbulence decay during the latter part of uprush and the early part of the downwash phases; (iii) the phases dominated by the bed-generated turbulence, yielding the -1 spectral law during the latter part of the downwash phases (note that the -1 slope is apparent in the near-bed spatial spectrum most of the time in the swash zone).

The spatial evolution of the turbulence indicates that the shear-layer-generated turbulence grows from the outer to the inner surf zone regions. Shear-layer-generated turbulence is insignificant once the bore collapses in the swash zone. The bed-generated turbulence is more important in the swash zone, during both the uprush and the downwash.

Spectral analysis reveals that the turbulence is evolving towards the two-dimensional as the bore front propagates onshore. It is believed that the time scale (the time between bore fronts and their phasing with respect to the maximum run-up) is the critical factor determining whether two-dimensional turbulence develops in the swash zone. In this study, the time scale is not sufficiently long for two-dimensional turbulence to be fully developed in the swash zone, but there is evidence from the spectra that the slope is approaching -3 at the lower wavenumbers at the bore front, characteristic of two-dimensional turbulence.

The comparison of turbulent production and dissipation shows that local equilibrium exists during the bore-front phase and near the bed during the latter part of the downwash phase in the outer surf zone as well as during the bore-front phase in the inner surf zone. The production is much smaller than the dissipation at the reversal phase and the early part of the downwash phase because of the lack of significant mean shear in the water column once the bore front passes the cross-shore location. Dissipation is dominant in the inner surf and swash zones during the downwash phase. The swash zone is primarily a dissipater.

The authors gratefully acknowledge the financial support of the National Science Foundation (grant no. OCE-0095834) and the Office of Naval Research (grant no. N00014-99-1-0193) for this research. The Office of Naval Research (grant no. N00014-99-1-0591) also supported the development of the PIV system. We are grateful to Professor Harry Yeh at the Oregon State University and Dr Britt Raubenheimer at Woods Hole Oceanographic Institution for suggestions on this work. I. M. Sou wishes to acknowledge the support from the National Science Foundation (grant nos CMS-0245206 and 0324498) and the Oregon State University's Edwards Endowment. P. L.-F. Liu wishes to acknowledge the support from the Alexander von Humboldt-Stiftung Foundation.

REFERENCES

- BATTJES, J. A. 1974 Surf similarity. In *Proceedings of the 14th Conference on Coastal Engineering*, pp. 466–480. ASCE.
- BEACH, R. A., & STERNBERG, R. W. 1992 Suspended sediment transport in the surf zone: response to incident wave and longshore current interaction. *Mar. Geol.* **108**, 275–294.
- CHANG, K.-A. & LIU, P. L.-F. 1999 Experimental investigation of turbulence generated by breaking waves in water of intermediate depth. *Phys. Fluids* **11**, 3390–3400.
- CHEN, D. & JIRKA, G. H. 1995 Experimental study of plane turbulent wakes in a shallow water layer. *Fluid Dyn. Res.* **16**, 11–41.
- COWEN, E. A. & MONISMITH, S. G. 1997 A hybrid digital particle tracking velocimetry technique. *Exp. Fluids* **22**, 199–211.
- COWEN, E. A., SOU, I. M., LIU, P. L.-F. & RAUBENHEIMER, B. 2003 Particle image velocimetry measurements within a laboratory generated swash zone. *J. Engng Mech.* **129**, 1119–1129.
- COX, D. T., HOBENSACK, W. & SUKUMARAN, A. 2000 Bottom shear stress in the inner surf and swash zone. In *Proceedings of the 27th International Conference of Coastal Engineering* (ed. B. L. Edge), pp. 108–119.
- DAVIDSON, P. A. 2004 *Turbulence: An Introduction for Scientists and Engineers*. Oxford University Press.
- DEAN, R. G. & DALRYMPLE, R. A. 1991 *Water Wave Mechanics for Engineers and Scientists*. World Scientific.
- DORON, P., BERTUCCIOLI, L., KATZ, J. & OSBORN, T. R. 2001 Turbulence characteristics and dissipation estimates in the coastal ocean bottom boundary layer from PIV data. *J. Phys. Oceanogr.* **31**, 2108–2134.
- EFRON, B. & TIBSHIRANI, R. 1993 *An Introduction to the Bootstrap*. Chapman and Hall.

- FENG, T. & STANSBY, P. K. 2005 Streamline topography in periodic surf zone waves from LDA measurements. *Measure. Sci. Technol.* **16**, 1929–1936.
- GEORGE, R., FLICK, R. & GUZA, R. T. 1994 Observations of turbulence in the surf zone. *J. Geophys. Res.* **99**, 801–810.
- HWUNG, H. H., HWANG, K. S., CHIANG, W. S. & LAI, C. F. 1998 Flow structures in swash zone. In *26th International Conference on Coastal Engineering*, Reston, VA.
- KRAICHMAN, R. H. 1967 Inertial ranges in two-dimensional turbulence. *Phys. Fluids* **11**, 265–277.
- MEI, C. C. 1989 *The Applied Dynamics of Ocean Surface Waves*. World Scientific.
- MELVILLE, W. K., VERON, F. & WHITE, C. J. 2002 The velocity field under breaking waves: coherent structures and turbulence. *J. Fluid Mech.* **454**, 203–233.
- NADAOKA, K. & KONDOH, T. 1982 Laboratory measurements of velocity field structure in the surf zone by LDV. *Coastal Engng Jpn* **25**, 125–145.
- NIKORA, V. 1999 Origin of the -1 spectral law in wall-bounded turbulence. *Phys. Rev. Lett.* **83**, 734–736.
- PEDERSEN, C., DEIGAARD, R. & SUTHERLAND, J. 1998 Measurements of the vertical correlation in turbulence under broken waves. *Coastal Engng* **35**, 231–249.
- PETTI, M. & LONGO, S. 2001 Turbulence experiments in the swash zone. *Coastal Engng* **43**, 1–24.
- POPE, S. B. 2000 *Turbulent Flows*. Cambridge University Press.
- PULEO, J. A. & HOLLAND, K. T. 2001 Estimating swash zone friction coefficient on a sandy beach. *Coastal Engng* **43**, 25–40.
- RAUBENHEIMER, B., ELGAR, S. & GUZA, R. T. 2004 Observations of swash zone velocities: a note on friction coefficients. *J. Geophys. Res.* **109**, C01027.
- SOU, I. M. 2006 An experimental investigation of the turbulence structure within the surf and swash zones. PhD dissertation, Cornell University, Ithaca, NY.
- STANSBY, P. K. & FENG, T. 2005 Kinematics and depth-integrated terms in surf zone waves from laboratory measurement. *J. Fluid Mech.* **529**, 279–310.
- SVENDSEN, I. A. 1987 Analysis of surf zone turbulence. *J. Geophys. Res.* **92**, 5115–5124.
- TAYLOR, G. I. 1938 The spectrum of turbulence. *Proc. R. Soc. Lond. A* **164**, 476–490.
- TENNEKES, H. & LUMLEY, J. L. 1972 *A First Course in Turbulence*. MIT Press.
- TING, F. C. K. & KIRBY, J. T. 1994 Observation of undertow and turbulence in a laboratory surf zone. *Coastal Engng* **24**, 51–80.
- TING, F. C. K. & KIRBY, J. T. 1995 Dynamics of surf-zone turbulence in a strong plunging breaker. *Coastal Engng* **24**, 177–204.
- TING, F. C. K. & KIRBY, J. T. 1996 Dynamics of surf-zone turbulence in a spilling breaker. *Coastal Engng* **27**, 131–160.
- UIJTTEWAAL, W. S. J. & BOOIJ, R. 2000 Effects of shallowness on the development of free-surface mixing layers. *Phys. Fluids* **12**, 392–402.
- UIJTTEWAAL, W. S. J. & JIRKA, G. H. 2003 Grid turbulence in shallow flows. *J. Fluid Mech.* **489**, 325–344.
- WERELEY, S. T. & MEINHART, C. D. 2001 Second-order accurate particle image velocimetry. *Exp. Fluids* **31**, 258–268.
- WESTERWEEL, J. 1994 Efficient detection of spurious vectors in particle image velocimetry data sets. *Exp. Fluids* **16**, 236–247.